Inorganic Chemistry

pubs.acs.org/IC

Article

Bulky (Imino)phosphide and Mixed Bis-dimethyl-siloxane /(Imino)phosphide-supported Redox-Active Cu_5 and Cu_6 Nanoclusters: Luminescence and Photocatalytic Studies

Asutosh Patra, Kishor Shinde, Sourav Mandal, Ashwath Kudlu, Wei-dan Si, Maria Francis, Aloke Das,* Di Sun,* and Sudipta Roy*

Cite This: https://doi.org/10.1021/acs.inorgchem.5c03056

Read Online

ACCESS | Metrics & More | Article Recommendations | Supporting Information

ABSTRACT: Herein, we depict isolation of neutral air-stable atomically precise Cu_5 $[((R_2\text{-cAI})P(Dipp))_3Cu_5Cl_2]$ (cAI = cyclic alkyl(imino); Dipp = 2,6-diisopropylphenyl; R_2 = Cy (**2a**) and Et_2 (**2b**)) and Cu_6 $[((Et_2\text{-cAI})P(Dipp))_2Cu_6(OSiMe_2OSiMe_2O)_2]$ (**3**) nanoclusters, stabilized by bulky (imino)phosphide and mixed bis-dimethyl-siloxane/(imino)phosphide ligands. **2a−2b** and **3** are structurally characterized by X-ray single-crystal diffraction and studied by XPS, FT-IR, and NMR spectroscopy. **2a−2b** exhibit yellow emission at ambient temperature with photoluminescence quantum yields (ϕ_{PL}) up to 11% and significantly high average lifetimes (τ_{av} = 38−110 μs). At 80 K, **2a−2b** exhibit red emission with 5-fold to ∼80-fold increased τ_{av} values (191 μs−8.32 ms). Time-dependent density functional theory calculations, along with natural transition orbital analyses, reveal that the singlet−triplet energy gap, $\Delta E(S_1-T_1)$ for **2a−2b** lies in the order of ∼0.2 eV, which is comparable with the experimentally obtained value of 0.16 eV, suggesting thermally activated delayed fluorescence (TADF). The spin−orbit coupling matrix (SOCM) calculations between different excited singlet and triplet states reveal significantly larger values (∼10−14 cm^{-1}), which, along with lower $\Delta E(S_1-T_1)$ values, possibly facilitate an efficient spin-flipping process, enabling TADF. **2a** is fabricated to a converted-LED and utilized as an excellent photocatalyst for regioselective [2 + 3] cycloaddition of aromatic alkynes and azides in the presence of a white LED, affording substituted triazoles (**6**) in good yields.

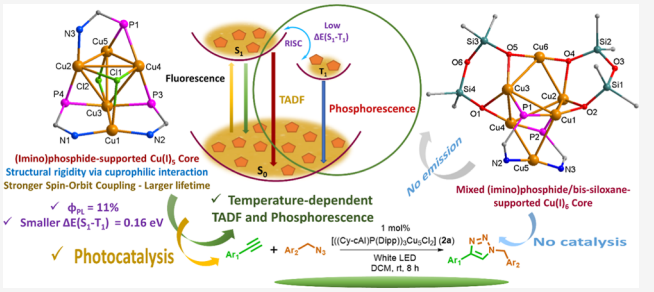

INTRODUCTION

Structurally well-defined metal clusters, stabilized by various ligand systems, have gained widespread importance owing to their various molecular properties, such as photoluminescence, catalysis, bioimaging, etc. The molecule-based optical materials are fascinating and captivating for efficient light harvesting and lighting purposes in modern electronic devices. However, applications of photoluminescent coinage metal clusters in designing organic light-emitting diodes (OLEDs)[1−6] are largely restricted due to their inherent lower stability. Among the various photophysical processes, phosphorescence involves emission from the lowest energy triplet excited state (T_1) to the singlet ground state (S_0). On the other hand, thermally activated delayed fluorescence (TADF) involves the emission from the lowest energy excited singlet state (S_1) to S_0 via intermediacy of the reverse intersystem crossing (RISC) from T_1 to S_1, provided the singlet−triplet energy gap, $\Delta E(S_1-T_1)$ is significantly smaller. This ensures a thermal equilibrium between the two excited states (S_1 and T_1), enabling effective RISC, and an increased radiative decay rate. For such thermally equilibrated excited states S_1 and T_1, the temperature dependence of the emission decay time can be expressed by the Boltzmann equation (eq 1) derived from the TADF model, as given below.[7]

$$\tau_{av} = \frac{3 + \exp\left[\frac{-\Delta E(S_1-T_1)}{k_B T}\right]}{\frac{3}{\tau(T_1)} + \left[\frac{1}{\tau(S_1)}\right]\exp\left[\frac{-\Delta E(S_1-T_1)}{k_B T}\right]} \quad (1)$$

where τ represents the experimentally obtained average lifetime, k_B is the Boltzmann constant, and T is the absolute temperature. The individual lifetime decays for the singlet and the triplet lowest excited states are given by $\tau(S_1)$ and $\tau(T_1)$, respectively. For an effective TADF to be in place, the $\Delta E(S_1-T_1)$ should be preferably less than 0.37 eV.[8] On the other hand, phosphorescence relies on larger spin−orbit coupling (SOC), common for precious transition metals with heavy-

Received: July 3, 2025
Revised: September 9, 2025
Accepted: September 26, 2025

atom effect, e.g., Pt^{II}, Ir^{III}, etc. In the case of TADF, the smaller value of $\Delta E(S_1-T_1)$ leads to poor spatial overlap between the wave functions of the S_1 and the S_0 states, resulting in a smaller oscillator strength for the respective $S_1 \rightarrow S_0$ transition, causing a longer singlet-state decay time, which brings in the saturation effect when applied in OLEDs. However, combining an additional radiative decay process from the lowest energy triplet state, i.e., phosphorescence, along with TADF could significantly enhance the overall rate of the radiative decay. This can be achieved by exploiting the polynuclear metal clusters, which can exhibit larger SOC induced by the presence of multiple metal centers. Stabilization of structurally precise polynuclear metal clusters depends on the steric and electronic environments induced by the stabilizing ligands, which in turn play a crucial role in controlling various molecular properties. In recent times, there has been a huge interest observed among synthetic chemists to employ such metal clusters as homogeneous catalysts for various organic transformations affording pharmaceutically relevant small molecules. The most prominent ligand systems identified to date for the stabilization of Cu(I)-based clusters include: alkynes, carboxylates, cyanurate, hydrides, phosphines, sulfides, and thiolates.[9−13] Ligands with soft donor sites, such as phosphines, bind the metal centers weakly, increasing the lability; whereas the ligands with hard donors, e.g., alkynes, thiolates, etc., approach the metal centers with unalterable binding modes, enabling metal exchange, resulting in a lower stability. Herein, we report on the first syntheses and structural characterization of bulky (imino)phosphide[14] and mixed bis-dimethyl-siloxane/(imino)-phosphide-stabilized robust air-stable, neutral Cu_5 (**2a−2b**), and Cu_6 (**3**) metal NCs, which have been further characterized by XPS, FT-IR, UV−vis, NMR spectroscopy, and mass spectrometry. The photocatalytic properties of **2a−2b** have been explored by taking advantage of their exciting temperature-dependent photoluminescence along with significant SOC, longer lifetimes, and moderately high quantum yields.

RESULTS AND DISCUSSION

Three equivalent of bulky (imino)phosphide ligand $[((R_2\text{-cAI})P(Dipp))_2Cs_2(THF)_4]_n$ (**1**)[14] (cAI = cyclic alkyl(imino); Dipp = 2,6-diisopropylphenyl; R_2 = Cy (**1a**), Et_2 (**1b**)) was reacted with 5 equiv of anhydrous CuCl in THF at room temperature (rt) under an argon atmosphere to obtain dark yellow filtrate of Cu_5 nanoclusters (NCs) $[((R_2\text{-cAI})P(Dipp))_3Cu_5Cl_2]$ (R_2 = Cy (**2a**), Et_2 (**2b**)). The yields of isolated pure crystals of **2a−2b** are found to be 51 and 53%, respectively (Scheme 1).

On the other hand, the reaction of a 1:1 molar ratio of **1b** and CuCl in the presence of silicone grease,[15] afforded the yellow needles of mixed bis-dimethyl-siloxane/(imino)-phosphide-supported Cu_6 NC $[((Et_2\text{-cAI})P(Dipp))_2Cu_6(OSiMe_2OSiMe_2O)_2]$ (**3**) in 42% yield via activation of polymeric silicone grease in the presence of the highly reactive (imino)phosphide nucleophiles (Scheme 1). **2a−2b** and **3** are found to be thermally stable up to 172−173 °C (**2a**), 175−176 °C (**2b**), and 256 °C (**3**). The thermal stability of the reported NCs was also studied by thermogravimetric analyses (TGA) (see Supporting Information). The crystals of were stable for several months in open air under ambient conditions. The +1-oxidation state of the Cu centers in the isolated clusters has been confirmed by the X-ray photoelectron spectroscopy (see Supporting Information) were further characterized by ESI-MS studies.

Scheme 1. Syntheses of NCs $[((Cy\text{-cAI})P(Dipp))_3Cu_5Cl_2]$ (2a), $[((Et_2\text{-cAI})P(Dipp))_3Cu_5Cl_2]$ (2b), and $[((Et_2\text{-cAI})P(Dipp))_2Cu_6(OSiMe_2OSiMe_2O)_2]$ (3)[a]

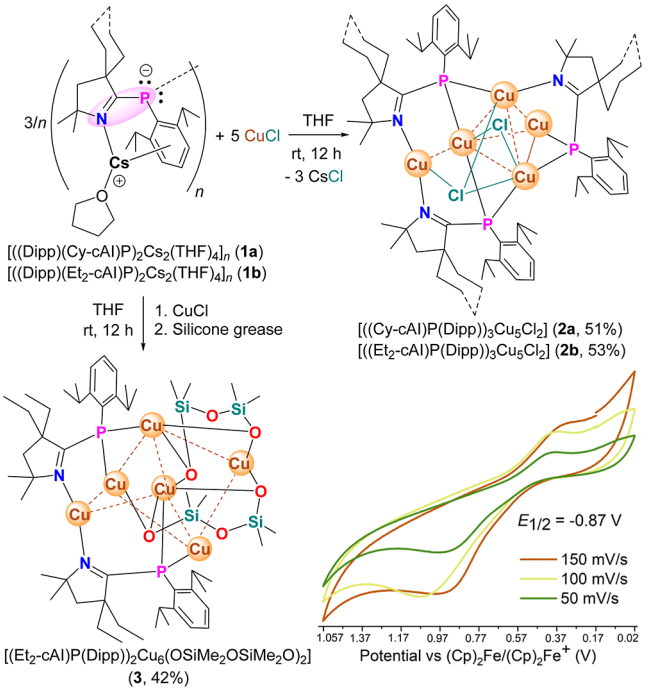

[a]Inset: cyclic voltammograms of **2a** in THF containing 0.1 M $[n\text{-}Bu_4N]PF_6$ as the electrolyte (CE: Pt, WE: GC, RE: Ag).

The ^{31}P NMR spectra of **2a** and **2b** in DCM-D_2, exhibited one quartet and two doublets at −66.1 (dd, J = 105.3, 42.1 Hz), −73.0 (d, J = 98.8 Hz), and −99.2 (d, J = 140.9 Hz) ppm for **2a**; and −67.0 (dd, J = 138.1, 94.5 Hz), −72.3 (d, J = 101.7 Hz), and −97.1 (d, J = 130.8 Hz) ppm for **2b**, respectively, suggesting the presence of three chemically different P atoms. The ^{13}C NMR spectrum of **2a** showed a doublet at 195.7 ppm (J_{C-P} = 89.8 Hz) representing the $C_{N=C}$ atom, which is slightly upfield shifted compared to that of **1a** (199.2 ppm, d, J_{C-P} = 73.7 Hz). Similarly, the ^{13}C NMR spectrum of **2b** exhibited a doublet at 196.2 ppm (J_{C-P} = 108 Hz), representing the $C_{N=C}$ atom. The ^{31}P and ^{29}Si NMR spectra of **3** in DCM-D_2 exhibited singlets at 7.6 and −21.8 ppm, respectively. The cyclic voltammetry (CV) studies of a THF solution of **2a** containing 0.1 M $[n\text{-}Bu_4N]PF_6$ as the electrolyte exhibited a quasi-reversible one-electron reduction at $E_{1/2}$ in the range of −0.87 V (potential vs $(Cp)_2Fe/(Cp)_2Fe^+$, used as a reference) at various scan rates (Scheme 1, inset). Cluster **3** was found to be redox-inactive under similar conditions.

The NCs **2a−2b** and **3** are structurally characterized by single-crystal X-ray diffraction. **2a−2b** crystallize in $P\text{-}1$ and $P2_1/n$ space groups, respectively. Considering the structural similarities of **2a** and **2b**, the structures of only **2a** and **3** are described here. The molecular structures of **2a−2b** and **3** are depicted in Figures 1 and 3, respectively. The pentanuclear Cu(I)-cluster (**2a**) comprises three monoanionic PN-donor (imino)phosphide ligands $[(Cy\text{-cAI})P(Dipp)]^-$, five Cu(I) ions, and two Cl^- ions. A distorted $Cu(I)_4$ tetrahedron (Cu2, Cu3, Cu4, Cu5) in the center of **2a** is stabilized via three μ-P bridging atoms of three (imino)phosphide ligands, one μ-Cl, and one μ_3-Cl anion. The Cu2 atom of this tetrahedron is further coordinated by one of the N atoms of the (imino)-

https://doi.org/10.1021/acs.inorgchem.5c03056
Inorg. Chem. XXXX, XXX, XXX−XXX

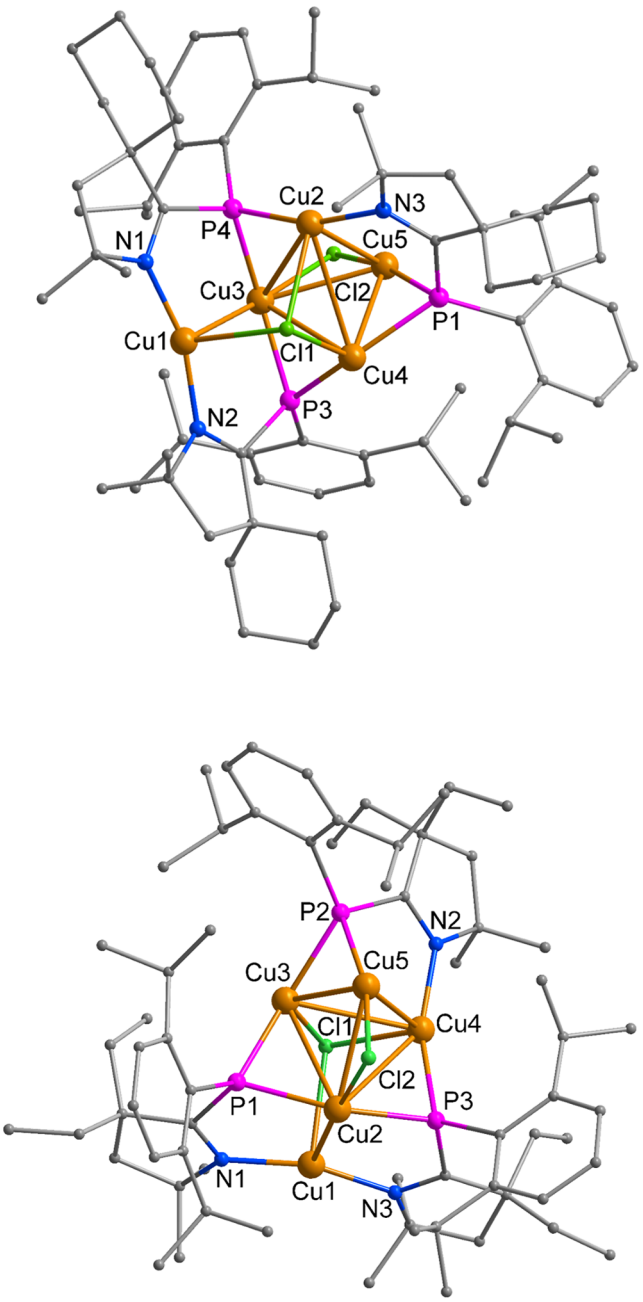

Figure 1. Top: molecular structure of $[((Cy\text{-}cAI)P(Dipp))_3Cu_5(Cl)_2]$ (**2a**). Selected experimental and computed [calculated at B3LYP-D3BJ/def2-SVP] bond lengths [Å] and bond angles [°]: Cu1−Cu3 2.7804(8) [2.736], Cu2−Cu5 2.8018(8) [2.791], Cu2−P4 2.2106(13) [2.238], Cu3−Cu4 2.8977(8) [2.987], Cu3−Cu5 2.7591(8) [2.734], Cu3−P3 2.2286 (14) [2.247], Cu3−P4 2.2284(14) [2.249], Cu4−Cu5 2.6031(8) [2.639], Cu4−P1 2.2523 (13) [2.287], Cu4−P3 2.2651(14) [2.287], P3−C17 1.819(5) [1.816], N2−C17 1.299(6) [1.293], N2−C17−P3 118.1(4) [118.7]. Bottom: molecular structure of $[((Et_2\text{-}cAI)P(Dipp))_3Cu_5(Cl)_2]$ (**2b**). Selected experimental and computed [calculated at B3LYP-D3BJ/def2-SVP] bond lengths [Å] and bond angles [°]: Cu2−Cu3 2.8864(4) [2.978], Cu2−Cu5 2.7566(4) [2.718], Cu2−Cu1 (2.7385 4) [2.706], Cu2−P1 2.2426(6) [2.261], Cu2−P3 2.2406(6) [2.259], Cu3−Cu5 2.5851(4) [2.654], Cu3−P2 2.2677(6) [2.280], Cu3−P1 2.2774(6) [2.286], Cu4−Cu5 2.8222(4) [2.755], P1−C1 1.828(2) [1.827], N1−C1 1.285(3) [1.290], N1−C1−P1 118.05(16) [118.3]. Hydrogen atoms and DCM solvent (for **2b**) are omitted for clarity.

phosphide ligand $[(Cy\text{-}cAI)P(Dipp)]^-$ ($\eta^1{:}\eta^2{:}\mu_3$), while the two other N atoms from the other two ligands are linearly coordinated to Cu1. The central core of **2a** remains intact due to one μ_3-bridged Cl1, holding Cu1, Cu2, Cu4, and μ_2-bridged Cl2, holding Cu5 and Cu3 atoms.

The Cu···Cu interactions found in **2a** vary from 2.6031(8)−2.8018(8) Å, which are shorter than the sum of the van der Waals radii (2.80 Å) and therefore can be considered as a closed-shell d^{10}−d^{10} cuprophilic interaction,[16] comparable to those of the clusters $[((Et_2\text{-}cAI)P(Dipp))_3Cu_4Cl]$[13] (2.6181(6) Å), $[Cu_9\{(py)_2im\}_2(PhCuC)_4(CF_3CO_2)_4](PF_6)$ (2.497(1)-2.741(1) Å (with an average of 2.574 Å)).[17] The average Cu−P bond distance in **2a** is found to be 2.242 Å, which is longer than that of $[((Et_2\text{-}cAI)P(Dipp))_3Cu_4Cl]$ (2.4098(7) Å),[14] but comparable with $\{[IMes{\cdot}PPh](CuCl)_2\}_4$ (2.1828(7)−2.2110(7) Å).[18] The P3−C17 and C17−N2 bond lengths are found to be 1.819(5) and 1.299(6) Å, respectively. The calculated (at B3LYP-D3BJ/def2-SVP level of theory)[19−21] bond parameters of **2a** are in well agreement with those obtained experimentally (Figure 1, see Supporting Information). The generated Hirshfeld surface and fingerprint plots[22] of **2a**−**2b** revealed significant Cu···Cu interactions (see Supporting Information).

The space-filling view of **2a** represents the well-protected central Cu_5 metallic cores by the aromatic and aliphatic groups of the respective ligands (Figure 2, left). The molecular electrostatic potential (MEP) plot (Figure 2, right) of **2a** shows that charge accumulation at the inorganic $P_3Cu_5Cl_2$ core is higher than that at other parts of the complex. The electron excitation from this core to π^*-orbitals of three N═C units is most likely to occur under photoirradiation. Structural analysis reveals that both Cu_5 clusters **2a** and **2b** have comparable bond parameters, except the Cu−Cu distances within the tetrahedral core of the NCs, which vary in the range of 2.58−3.04 Å (see Supporting Information for detailed structural description of **2b**).

The hexanuclear Cu(I)-cluster, **3** crystallizes in $P2_1/n$ space group and comprises of six Cu(I) centers, supported by two $[(Et_2\text{-}cAI)P(Dipp)]^-$ ligands and two dianionic bis-dimethyl-siloxane ligands (Figure 3). The latter originated in situ via activation of silicone grease.[15] The Cu−O inorganic core of **3** consists of a distorted Cu_4 unit (Cu1, Cu2, Cu3, and Cu4). The Cu(I) ions present in **3** are bridged by four μ_2-O atoms derived from two dianionic chelating $[^-O{-}Si(Me_2){-}O{-}Si(Me_2){-}O^-]$ ligands ($\eta^2{:}\eta{:}^2\mu_4$). The $Cu_4{-}(\mu\text{-}O)_4$ unit is capped from opposite sides by the remaining two copper atoms (Cu5 and Cu6). Notably, no chloride bridges are observed between the central Cu_6 core of **3** unlike those of **2a**−**2b**. The Cu···Cu distances in **3** range from 2.6434(4)−3.0007(4) Å, which are comparatively longer than those of **2b** (2.5851(4)−3.0482(5) Å). Each Cu atom in the Cu_4 core of **3** is stabilized by two $(Et_2\text{-}cAI)P(Dipp)$ ligands, with Cu−P distances ranging from 2.1570(6) to 2.1824(7) Å. Notably, the Cu−P bond lengths in **3** are slightly shorter than those of **2b** (2.2011(6)−2.2774(6) Å). It is important to mention that the Cu atoms in the Cu_5 NCs are coordinated by the N atoms of the two (imino)phosphide ligands $(Et_2\text{-}cAI)P(Dipp)$, while in Cu_6 NC (**3**), the Cu atoms are solely coordinated through oxygen atoms of the bis-dimethyl-siloxane ligands.

Photophysical Studies. Interestingly, the pure crystals and powders of **2a**−**2b** were found to exhibit bright yellow emission at ambient temperature (300 K) and red emission at 80 K (using a liquid nitrogen bath, see Supporting

https://doi.org/10.1021/acs.inorgchem.5c03056
Inorg. Chem. XXXX, XXX, XXX−XXX

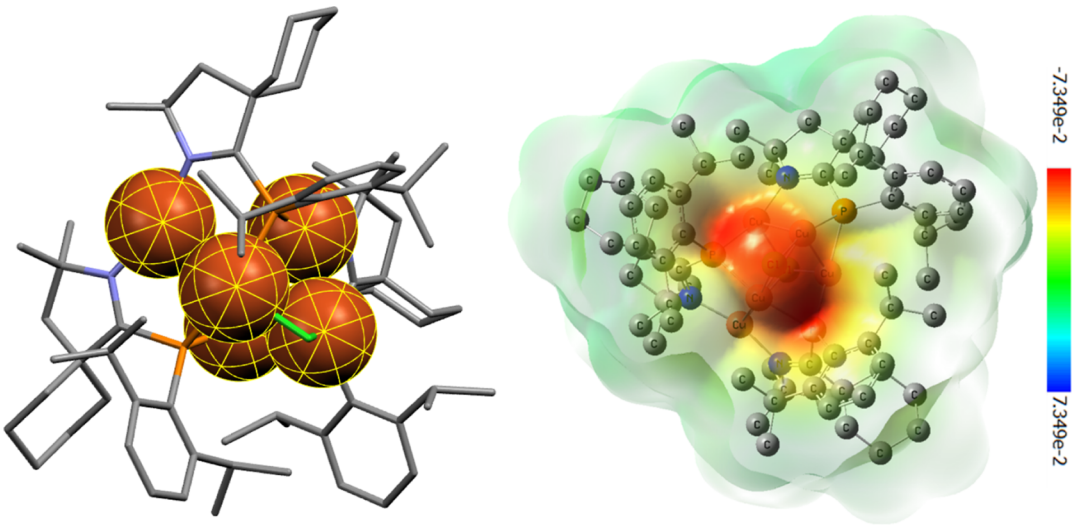

Figure 2. Left: space-filling view of the Cu_5 metallic core. Right: MEP plot of NC $[((Cy\text{-}cAI)P(Dipp))_3Cu_5(Cl)_2]$ (**2a**), calculated at B3LYP-D3BJ/def2-SVP level of theory.

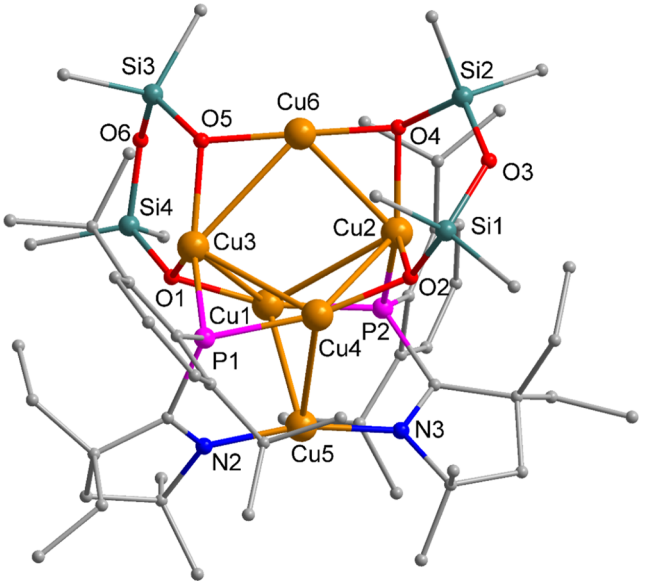

Figure 3. Molecular structure of $[((Et_2\text{-}cAI)P(Dipp))_2Cu_6(OSiMe_2OSiMe_2O)_2]$ (**3**). Hydrogen atoms are omitted for clarity. Selected experimental bond lengths [Å] and bond angles [°]: Cu1−Cu2 2.8592(4), Cu1−Cu3 2.8049(4), Cu1−Cu5 2.7404(4), Cu1−P1 2.1570(6), Cu1−O2 1.8556(16). Cu2−Cu4 3.0007(4), Cu2−Cu6 2.6434(4), Cu2−P2, 2.1645(6), Cu3−Cu4 2.7684(4), Cu3−Cu6 2.8867(4), Cu5−N2 1.8788(19), Cu5−N3 1.8813(19), P1−C8 1.812(2), P2−C16 1.822(2), Cu4−Cu5−Cu1 74.721(11), Cu2−Cu6−Cu3 89.026(12).

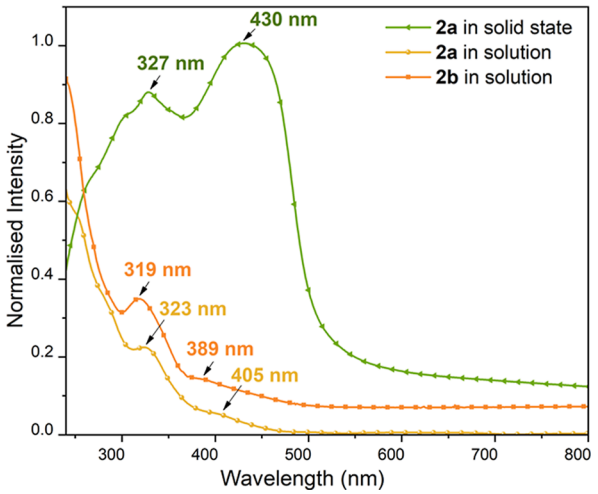

Figure 4. Normalized UV−vis absorption spectrum of $[((Cy\text{-}cAI)P(Dipp))_3Cu_5Cl_2]$ (**2a**) in DCM solution (yellow) and $[((Et_2\text{-}cAI)P(Dipp))_3Cu_5Cl_2]$ (**2b**) in DCM solution (orange), and diffused reflectance spectrum of $[((Cy\text{-}cAI)P(Dipp))_3Cu_5Cl_2]$ (**2a**) in solid state (green) at 298 K. The absorption bands were observed at 323 and 405 nm for **2a**, 319 and 389 nm for **2b** (in DCM), and 327 and 430 nm for **2a** (solid-state), respectively.

Information) under the laboratory UV lamp of 365 nm wavelength. In contrast, cluster **3** was found to be nonemissive under similar conditions both in solution and in the solid state. We performed detailed investigations of the photophysical properties of **2a**−**2b** (Figures 4−8, see Supporting Information). The UV−vis absorption spectra of DCM solutions of **2a**−**2b** (Figure 4) recorded at ambient temperature (300 K) under an argon atmosphere exhibited the absorption maxima (λ_{max}) at 323 nm with a shoulder at 405 nm (for **2a**) and λ_{max} at 319 nm with a shoulder at 389 nm (for **2b**). The photoluminescence (PL) spectrum of the same DCM solution of **2a** at 300 K exhibited the emission band ranging from 500 to 850 nm with λ_{em} at 650 nm (see Supporting Information). The temperature-dependent emission spectra of **2a** in DCM solution exhibited a sharp decrease in the emission intensities with the increase of temperature from 200 to 300 K, with a blue shift from 680 to 650 nm (see Supporting Information). The average lifetime (τ_{av}) observed at 200 K was 14.1 μs (see Supporting Information).

The UV−vis diffused reflectance spectrum of **2a** in the solid state exhibited two broad bands at 300 K, ranging from 250 to 500 nm approximately, with the corresponding λ_{max} values at 327 and 430 nm, respectively (Figure 4).

The estimated photoluminescence quantum yields (PLQY, ϕ_{PL}) of **2a**−**2b** in the solid state at 300 K were found to be 11 and 5%, respectively.

To have a deeper knowledge of the excited state transitions, we recorded the PL spectra of **2a** in pure powder form at various temperatures, ranging from 80 to 300 K (Figure 5). A

https://doi.org/10.1021/acs.inorgchem.5c03056
Inorg. Chem. XXXX, XXX, XXX−XXX

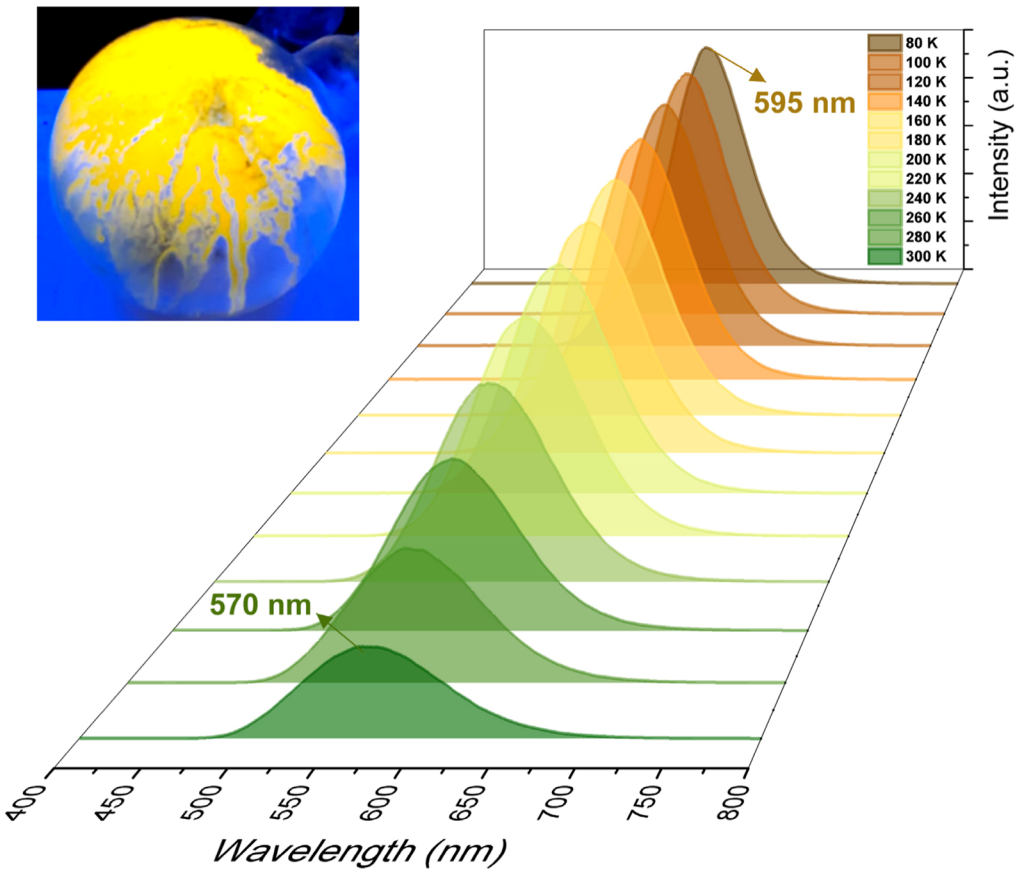

Figure 5. Temperature-dependent photoluminescence (PL) spectra of $[((Cy\text{-}cAI)P(Dipp))_3Cu_5Cl_2]$ (**2a**) in the solid state at 370 nm of excitation wavelength. **Inset:** powder form of the pure crystals of **2a** under laboratory UV lamp of wavelength 365 nm.

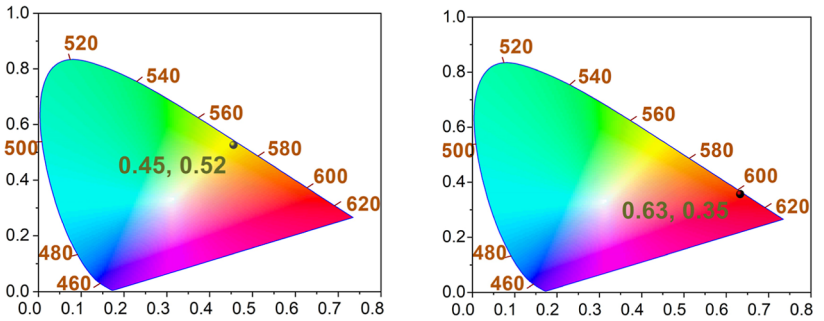

Figure 6. Photoluminescence color coordinates of $[((Cy\text{-}cAI)P(Dipp))_3Cu_5Cl_2]$ (**2a**) at 300 K (left) and at 200 K (right), plotted in the CIE 1931 chromaticity diagram. The gray dots correspond to the coordinates attributed to yellow-light emission (0.45, 0.52), and red-light emission (0.63, 0.35), respectively.

gradual decrease in the emission intensity of the PL spectra was observed by increasing the temperature from 80 K (λ_{em} = 595 nm) to 300 K (λ_{em} = 570 nm) with a blue shift (25 nm) in the respective λ_{em} maxima (Figure 5, see Supporting Information),[17,22] suggesting a TADF process.[23]

Conversely, the temperature-dependent PL spectra of **2b** exhibited a progressive enhancement in emission intensity as the temperature decreased from 300 K (λ_{em} = 579 nm) to 80 K (λ_{em} = 571 nm), accompanied by a blue shift of 8−9 nm in the emission maximum (Figures S30 and S31).

The photoluminescence color coordinates of **2a** at 300 K (Figure 6, left) and at 200 K (Figure 6, right), plotted in the CIE 1931 chromaticity diagram, are represented in Figure 6, which shows a transition in the emission property from yellow at 300 K to red at 200 K. A similar transition is also seen for **2b** (see Supporting Information).

The temperature-dependent lifetime decay (performed on a solid sample of **2a**) plots for **2a** showed the biexponential nature with more than a 5-fold increase in the average lifetime, τ_{av} from 38.1 (at 300 K) to 191.1 μs (at 80 K), suggesting emissions that originate from two different excited states, i.e., S_1 and T_1, which are in thermal equilibrium (Figure 7, top). A similar phenomenon was also observed for **2b** (see Supporting Information) with a dramatic increase of the τ_{av} values by about seventy-five times from 110 μs (at 300 K) to 8.32 ms (at 80 K) (Table S4, see Supporting Information), indicating the dominance of phosphorescence at lower temperature.

https://doi.org/10.1021/acs.inorgchem.5c03056
Inorg. Chem. XXXX, XXX, XXX−XXX

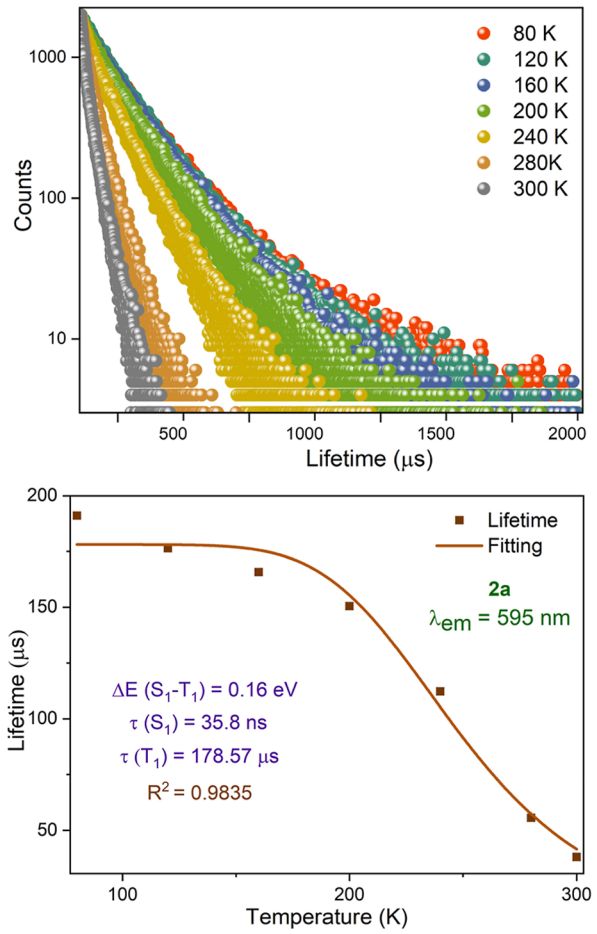

Figure 7. Top: temperature-dependent lifetime decay plot of $[((Cy\text{-}cAI)P(Dipp))_3Cu_5Cl_2]$ (**2a**) in solid state (λ_{em} = 570 nm and λ_{ex} = 310 nm). Bottom: lifetime vs temperature plot for $[((Cy\text{-}cAI)P(Dipp))_3Cu_5Cl_2]$ (**2a**) in solid state (λ_{em} = 595 nm).

The fitting of the temperature-dependent PL decay plots of **2a**–**2b** to the eq 1 afforded the $\Delta E(S_1-T_1)$ values of 0.16 and 0.050 eV, respectively, with the coefficients of determination, $(R)^2$ values of 0.983 (**2a**) and 0.993 (**2b**), confirming the TADF nature (Figure 7, bottom; see Supporting Information for **2b**).

The radiative lifetime values of **2a**–**2b**, derived from the fittings to eq 1, were found to be $\tau(S_1)$ = 35.8 ns (**2a**), 17.67 μs (**2b**); $\tau(T_1)$ = 178.57 μs (**2a**), 9.20 ms (**2b**), respectively (see Supporting Information). The fitted $\tau(T_1)$ value (178.57 μs) of the lifetime vs T plot of **2a** was observed to be very close to the experimentally obtained value of 176.4 μs at 120 K. Similarly, the fitted $\tau(T_1)$ value (9.20 ms) of the lifetime vs T plot of **2b** was observed to be very close to the experimentally obtained value of 8.32 ms at 80 K.

To confirm the presence of phosphorescence at lower temperature, a well-established phenomenon exhibited by Cu(I)-based metal complexes/clusters due to the higher spin–orbit coupling (SOC), enabling effective transition from $T_1 \rightarrow S_0$ states,[24−26,29] we performed the spin–orbit coupling matrix element (SOCME) calculations for **2a**–**2b**, which showed significant coupling values (∼2–99 cm^{-1} and ∼12–84 cm^{-1}, respectively) for the S_1-T_n pairs, suggesting a fast ISC between two spin manifolds (Table S14 in Supporting Information).[27] This is further corroborated by the PL decay profile, which exhibits only μs scale components and lacks any prompt fluorescence, reinforcing the presence of a highly efficient ISC process (Figures 7 and 8). Moreover, the significantly higher SOCME values between T_1 and S_0 (27.12 cm^{-1} (**2a**), 17.96 cm^{-1} (**2b**)) states (Figure 8, Table S14 in Supporting Information) presumably accelerate the phosphorescence decay rates in **2a**–**2b**. To analyze the nature of the excited states, NTO calculations have been performed on **2a**–**2b** (Figure 8, right; see computational studies and Supporting Information).

The radiative rate constant of TADF (k_{S1}) was calculated to be 0.28 × 10^8 s^{-1} (**2a**) and 5.66 × 10^4 s^{-1} (**2b**). The significantly lower singlet–triplet energy gap and all other calculated and/or experimentally observed photophysical parameters unambiguously pointed toward the TADF nature of **2a**–**2b**.[25−28]

However, the reduced emission intensity at room temperature can be attributed to the higher rate of the nonradiative decay compared to that of the radiative decay, which was also confirmed by the respective k_r and k_{nr} values calculated as k_r = 0.28 × 10^4 s^{-1} (**2a**), 4.52 × 10^2 s^{-1} (**2b**), and k_{nr} = 2.33 × 10^4 s^{-1} (**2a**), 85.88 × 10^2 s^{-1} (**2b**) (Figure 7, bottom; see Supporting Information).

Toward the practical device application, we have fabricated the converted LED (c-LED) by physically applying a 5 mM solution of **2a** in a mixture of *n*-hexane and toluene on a commercially sourced InGaN UV-LED chip,[29] which exhibited excellent luminescence at 569 nm (Figure 9).

Computational Studies. To gain a deeper understanding of the electron density distribution and bonding analysis of the isolated NC **2a**, we have performed the geometry optimization of **2a**–**2b** at B3LYP-D3BJ/def2-SVP[18−20] level of theory (see

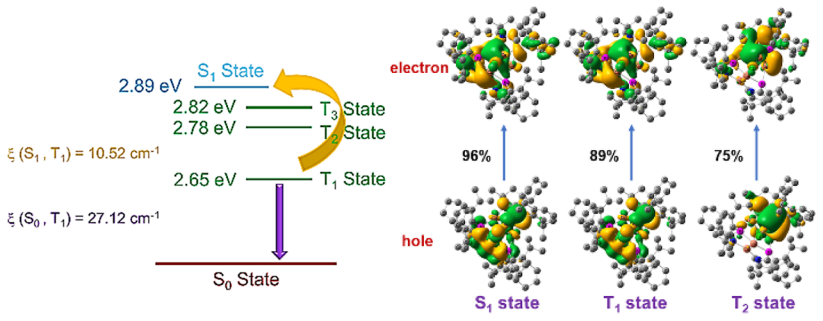

Figure 8. Left: energy diagram of **2a** obtained from single-point TD-DFT (50–50) calculation using TD-SCF method at B3LYP-D3BJ/def2-SVP level of theory. Right: natural transition orbital (NTO) analysis for low-lying S_1 and T_1–T_2 states of **2a**. Hole and electron pairs of S_1 and T_1–T_2 states of **2a** (see Supporting Information for details).

https://doi.org/10.1021/acs.inorgchem.5c03056
Inorg. Chem. XXXX, XXX, XXX−XXX

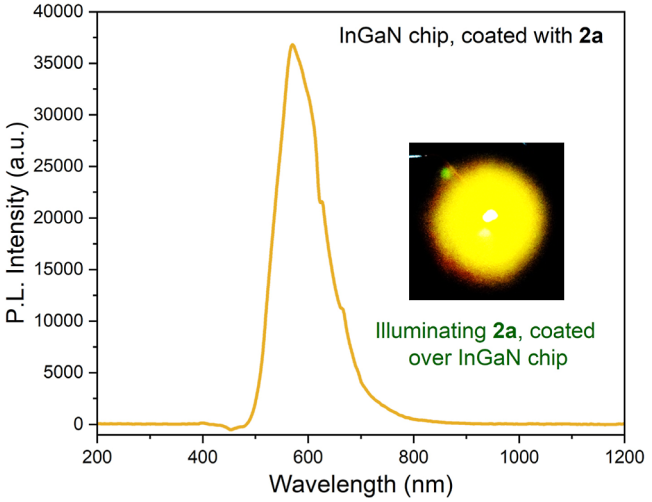

Figure 9. Luminescence spectrum of $[((Cy\text{-}cAI)P(Dipp))_3Cu_5Cl_2]$ (**2a**), coated over the InGaN chip, centered at the 390−395 nm region (λ_{em} = 569 nm and λ_{ex} = 390 nm). Inset: yellow luminescence of **2a** coated over InGaN chip after applying 3 V bias and 0.2 A current.

Supporting Information). The calculated bond parameters were found to be in accordance with the experimentally obtained values. The natural bond orbital (NBO) analysis[30−33] performed on the optimized coordinates of **2a** at B3LYP-D3BJ/def2-SVP level of theory showed the presence of a lone pair with p-character on each of the P atoms of the (aryl)-cyclic alkyl(imino) phosphide $[(Ar)(cAI)P]^-$ ligand and the presence of a 3-center-2-electron bond between the Cu−Cu−P moiety. The nature of the C_{cAAC}−P bond was found to be a single bond with a Wiberg Bond Index (WBI) of 1.05 in **2a**, and the C−N bond was found to have two bonding occupancies of 1.98e and 1.96e with a WBI of 1.65, suggesting a double bond nature. The HOMO, HOMO − 1, HOMO − 2, and HOMO − 3 represent the Cu−P interactions in **2a** (Figure 10).

The HOMO and HOMO − 2 represent the lone pair of electrons on the phosphorus atoms. The associative bonding interaction among the five Cu(I) ions and two Cl^- ions in the Cu_5Cl_2 core can be visualized from the HOMO − 4 (Figure 10). Moreover, HOMO − 4 does not involve the orbitals on the three P atoms. The σ-type interaction of Cu−N bonds, in which the bond is majorly polarized toward N (93%), is represented by HOMO − 8 and HOMO − 7 (see Supporting Information). The LUMO of **2a** represents the $\pi^*_{N=C\text{-}P}$ orbital (N1−C8−P4), π^*-orbital of one aromatic Dipp ring (at P1), and Cu···Cu interacting antibonding orbitals (Cu2···Cu5; **2a**).

The quantum theory of atoms in molecules analysis[34−36] of **2a** and **2b** provides significant insights into the nature of the Cu−Cu interactions present in these NCs (Figure 11, see Supporting Information).

For **2a**, the electron density ($\rho(r)$) at the bond critical points (BCPs) is found to be 0.027 au for the Cu1−Cu3 bond and 0.024 au for the Cu2−Cu5 bond, accompanied by the positive Laplacian values ($\nabla^2\rho(r)$) of 0.026 au and 0.025 au, respectively. In **2b**, the electron density ($\rho(r)$) values are 0.027 au for the Cu1−Cu5 bond and 0.025 au for the Cu3−Cu4 bond, with corresponding Laplacian values ($\nabla^2\rho(r)$) of 0.027 au and 0.025 au, respectively. The consistently positive Laplacian values across both **2a**−**2b** indicate a close−shell interaction, characteristic of electrostatic metal−metal bonding, rather than covalent bonding, as the electron density is depleted between the nuclei and concentrated toward the atomic cores. The relatively low G_b and $|V_b|$ values of kinetic (G) and potential (V) energy densities further support this conclusion.

The excited states for **2a** were calculated using time-dependent density functional theory (TD-DFT)[37,38] calculations at the B3LYP-D3BJ/def2-SVP level of theory. The

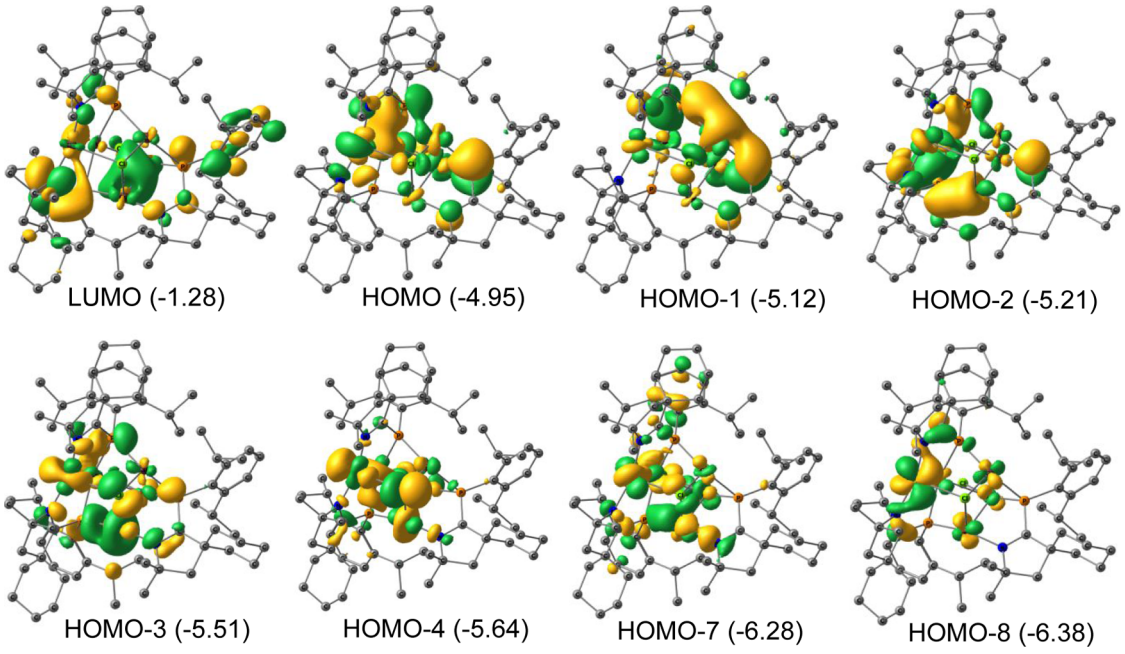

Figure 10. Selected Kohn−Sham orbitals of **2a**, representing Cu−P (HOMO, HOMO − 1, HOMO − 2, and HOMO − 3), and Cu−Cu (HOMO − 4) interactions (calculated at B3LYP-D3BJ/def2-SVP level of theory; energies given in parentheses are in eV). See Supporting Information for **2b**.

https://doi.org/10.1021/acs.inorgchem.5c03056
Inorg. Chem. XXXX, XXX, XXX−XXX

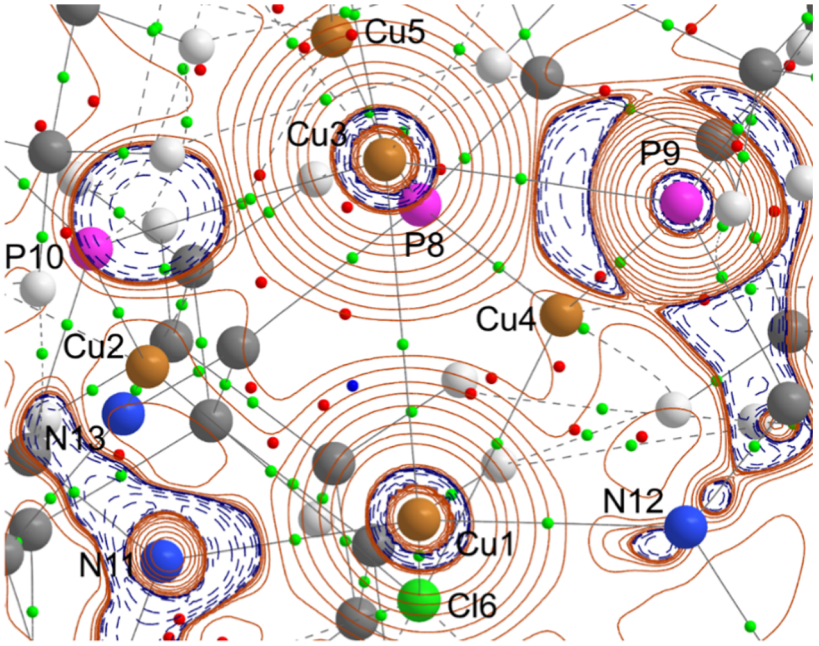

Figure 11. Contour plot of Laplacian distribution $[\nabla^2\rho(r)]$ in the Cu1−Cu3−P9 plane of **2a**. Solid blue lines indicate the areas of charge concentration ($\nabla^2\rho(r) < 0$), while dotted purple lines denote charge depletion ($\nabla^2\rho(r) > 0$). Solid lines connecting atomic nuclei (black) are the bond paths and green spheres on the bond path indicate the BCP. See Supporting Information for the Laplacian distribution of **2b**.

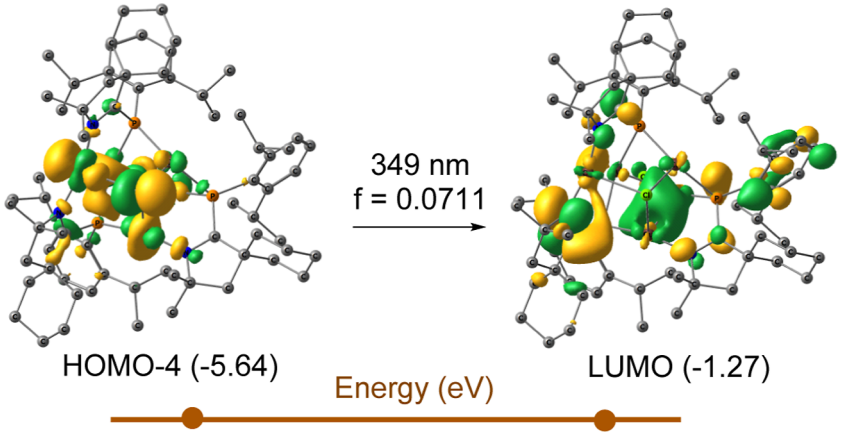

Figure 12. Calculated excitation energy for the absorption maxima and oscillator strength of **2a** at TD-B3LYP-D3BJ/def2-SVP level of theory in solvent (DCM) phase.

conductor-like solvation model, as developed in the polarizable continuum model framework, was used to implement the solvent (DCM) effect. For **2a**, in the DCM (solvent) phase, the electronic transition is attributed to the HOMO − 4 → LUMO transition, which corresponds to the transition from Cu−P to $\pi^*_{C=N}$, corroborating the absorption maximum appeared at an oscillator strength of f = 0.0711 (Figure 12).

The corresponding wavelength is found to be 349 nm, which is in good agreement with the experimentally observed λ_{max} value of 324 nm (for **2a**). For **2b**, the electronic transition is attributed to a HOMO − 2 → LUMO + 1, which corroborates the absorption maximum that appeared at the oscillator strength of f = 0.0598, corresponding to the wavelength of 349 nm (see Supporting Information). The calculated λ_{max} value for **2b** was also found to be in good agreement with the experimentally obtained absorption maximum (319 nm). NBO analyses suggest that the electronic transition from the cuprophilic Cu2···Cu5 unit to Cu1···Cu3 unit (HOMO − 4 to LUMO) is most likely responsible for phosphorescence, while a significant amount of intramolecular metal-to-ligand charge transfer transition can be visualized from the $Cu^I_5Cl_2$ core to $\pi^*_{N=C-P}$ orbital (N1−C8−P4), two $\pi^*_{N=C}$, π^* orbital of one aromatic Dipp ring (at P1), and the Cu···Cu interacting (2.80 Å) antibonding orbitals (Cu2···Cu5; **2a**), possibly facilitating the TADF process. Similar interactions are also observed from the respective Hirshfeld plots (see Supporting Information). The ^{1,3}MLCT transition in Cu_2Cl_2 stabilized by a couple of pyridyl-phosphine ligands was previously shown to be responsible for dual emission.[39] The absence of the significant coprophilic interactions comparable with **2a**−**2b** and the missing central chloride bridges are presumably responsible for the nonemissive nature of the Cu_6 cluster **3**.

The single-point TD-DFT calculations indicate that the low-lying excited states of **2a** and **2b** are energetically close, with small singlet−triplet energy gaps (ΔE_{ST}) of 0.24 and 0.22 eV, respectively (Figures S58−S60 in Supporting Information). To

https://doi.org/10.1021/acs.inorgchem.5c03056
Inorg. Chem. XXXX, XXX, XXX−XXX

Scheme 2. [((Cy-cAI)P(Dipp))$_3$Cu$_5$Cl$_2$] (2a)-Catalyzed Regioselective 1,2,3-Triazole (6) Syntheses in the Presence of White LED[a]

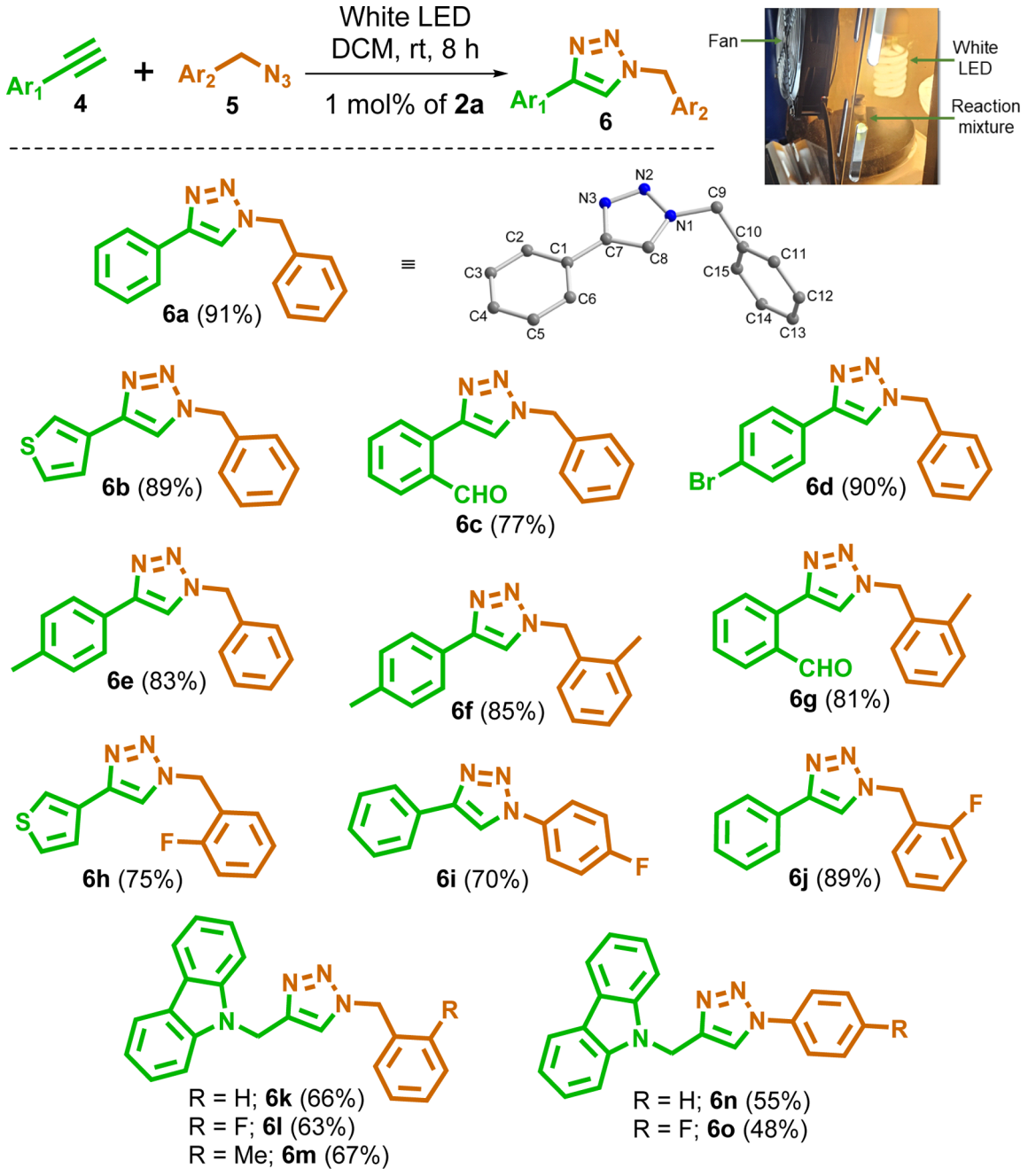

[a]Inset: Reaction setup under white LED.

analyze the nature of these excited states, NTO calculations were performed (Figures S58−S60 in Supporting Information). For the S_1 and T_1 states, the positions of the hole and electron are very similar, resulting in nearly identical electronic characteristics.[40] This is also reflected in the low SOCME[27] values (~10−14 cm^{-1}) between the S_1 and T_1 states for both **2a** and **2b**. However, the T_3 state of **2a** and the T_2 and T_3 states of **2b** exhibit different electronic characteristics compared to the S_1 state, as the positions of the hole and electron differ. This leads to enhanced SOCME values for the S_1-T_3 (~98 cm^{-1}) transition in **2a** and the S_1−T_2 (~84 cm^{-1}) as well as the S_1−T_3 (~30 cm^{-1}) transitions in **2b**, in accordance with the El-Sayed rule.[41] The combination of large SOCME values and small energy gaps between S_1−T_3 in **2a** and S_1−T_2/T_3 in **2b** opens alternative spin-flipping pathways mediated by higher triplet states. Consequently, in the case of TADF, triplet population transfer can occur via a hot RISC mechanism, where the transition from the T_2 or T_3 state to the S_1 state facilitates the process.

Photocatalytic Application of 2a. Atomically precise metal NCs are emerging materials that have recently attracted huge attention in homogeneous catalysis due to their unique structures, tunable compositions, and insightful structure−property correlations.[42] However, the catalytic applications of such NCs are still not widely explored, partly due to the inhibition of the catalytic sites by specially designed ligands,

https://doi.org/10.1021/acs.inorgchem.5c03056
Inorg. Chem. XXXX, XXX, XXX−XXX

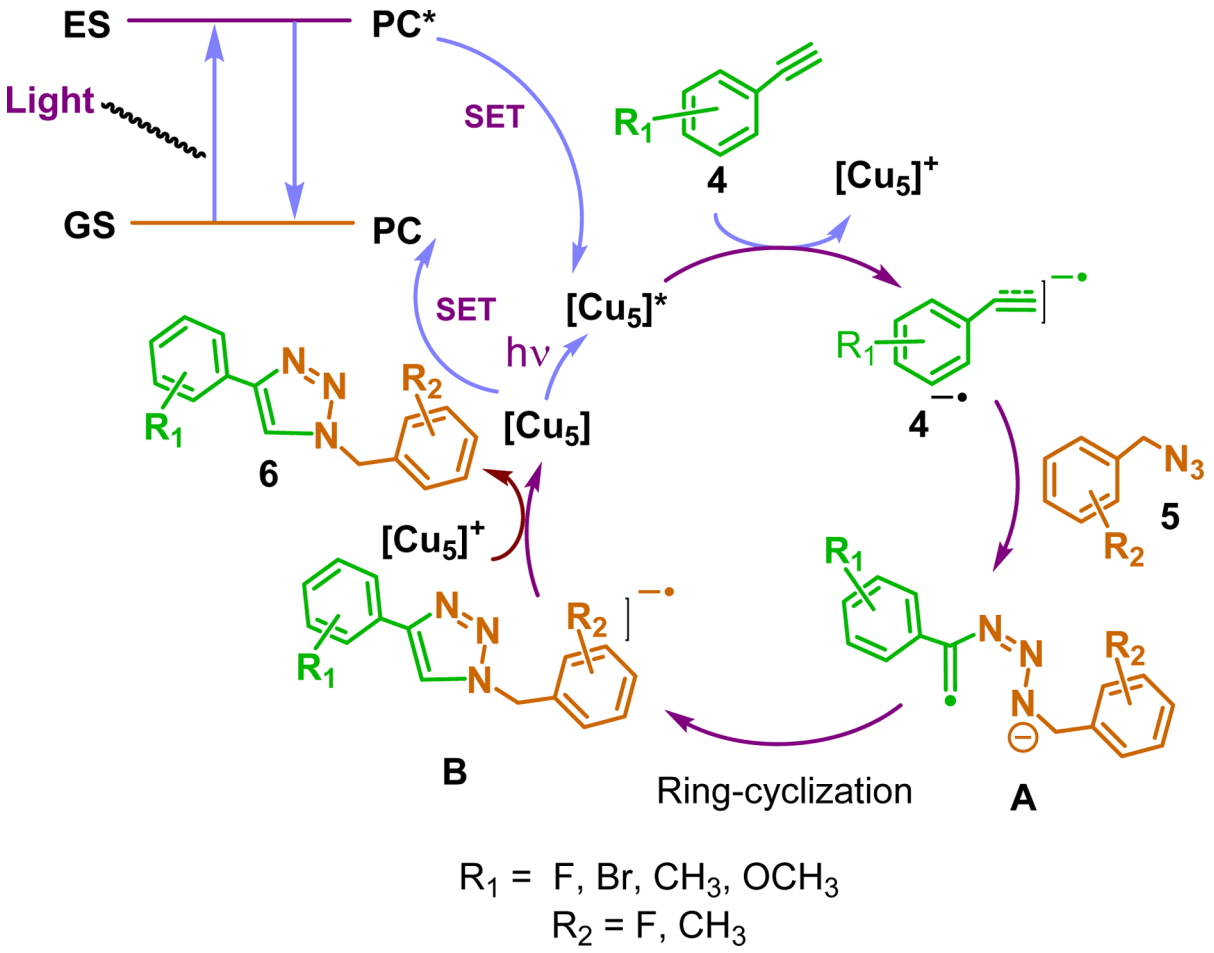

Figure 13. Plausible mechanism for the alkyne−azide cycloaddition reaction, catalyzed by **2a**.

which stabilize the structural cores. Catalytic alkyne−azide cycloaddition reactions[43−45] are very often limited by the low regioselectivity and reduced reaction rates at ambient temperature. Although an increase in the reaction temperature can speed up the reaction, the regioselectivity drops down giving rise to the formation of a mixture of 1,4- and 1,5-disubstituted triazoles.[46] Therefore, suitable catalytic systems are in high demand, which can yield regioselective products at ambient reaction conditions. Proving the excellent PL properties of redox-active pentanuclear Cu(I)-clusters, **2a**−**2b**, we explored their catalytic application for [3 + 2] cycloaddition of aromatic azides and alkynes. Optimization of initial reaction conditions revealed that the reaction of phenylacetylene (**4a**) and benzyl azide (**5a**) in the presence of 1 mol % of the NC **2a** as a catalyst at ambient temperature can afford the white solid of the corresponding 1-benzyl-4-phenyl-1*H*-1,2,3-triazole (**6a**) as the single regio-isomer in ∼20% yield after 24 h under household light source. The structure of **6a** was unambiguously confirmed by X-ray single-crystal diffraction.[47] When a similar reaction was performed under blue LED, **6a** was isolated in an increased yield of 72% with a reduced reaction time of 12 h (Table S16 in Supporting Information). However, **6a** was obtained with a much-improved yield of 91% after 8 h in the presence of a white LED without any loss of the regioselectivity (Scheme 2). Under a similar reaction condition, **6a** was obtained in a lower yield of 77% when 1 mol % the NC **2b** was utilized as the catalyst. Moreover, cluster **3** did not show any catalytic activity under similar reaction conditions. Having the optimized reaction conditions in hand, we further explored the substrate scope using various substituted aromatic alkynes (**4**) and azides (**5**). In all cases, we could successfully isolate the corresponding triazoles (**6b**−**6o**) in good to excellent yields (70−91%) and regioselectivity (Scheme 2).

We proposed a plausible single-electron transfer (SET) mechanism,[48] where the excited photocatalyst PC* ([Cu_5]* = **2a***) ($E_{1/2}$ = −0.5 V; Figure 1) under photoirradiation is proposed to transfer one electron to the alkyne **4a** ($E_{1/2}$ = 1.5 V) to form the corresponding radical anion (**4a**$^{\bullet-}$), which has been experimentally supported by the observation of a broad EPR signal near g = 2 at 298 K upon irradiation of the reaction mixture under the LED of 467 nm wavelength for 30 min (Figure 13; see Supporting Information). DFT calculations showed that the LUMO of alkyne **4a** is nearly 5 kcal/mol lower in energy than that of the aryl-azide **5a** ($E_{1/2}$ near −2.5 V), suggesting that the former is more prone to accept an electron from the catalyst (**2a***) under photocatalytic conditions (see Supporting Information). This highly reactive species **4a**$^{\bullet-}$ rapidly reacts with the azide **5a** to afford the intermediate **A**, which then undergoes a [2 + 3] cycloaddition to yield the triazolyl radical intermediate **B**. Subsequently, a single-electron oxidation of the intermediate **B** takes place by the oxidized form of the photocatalyst [$Cu(I)_5$]$^+$, furnishing the final 1,4-disubstituted 1,2,3-triazole product **6a** upon simultaneous regeneration of the photocatalyst [Cu_5], and thereby completing the catalytic cycle. The proposed SET mechanism was further experimentally proved by quenching of

https://doi.org/10.1021/acs.inorgchem.5c03056
Inorg. Chem. XXXX, XXX, XXX−XXX

the catalytic activity of **2a** in the presence of 1 equiv of TEMPO, resulting in the formation of only a trace amount of the expected product **6a** by treating **4a** and **5a** under optimized reaction condition (see Supporting Information). This photocatalytic approach offers an efficient and mild pathway for the synthesis of triazole derivatives under visible light irradiation.

CONCLUSION

In conclusion, we have demonstrated a facile synthetic route for the stabilization and solid-state isolation of three novel structurally well-defined air-stable metal NCs with Cu_5 (**2a**–**2b**) and Cu_6 (**3**) cores employing (aryl)-cyclic alkyl(imino) phosphides and mixed bis-dimethyl-siloxane/(imino)-phosphide ligands. **2a**–**2b** exhibited excellent temperature-dependent photoluminescence with combined phosphorescence at lower temperature, TADF at ambient temperature with photoluminescence quantum yields (ϕ_{PL}) up to 11%, and significantly longer average lifetimes (τ_{av}). Detailed photophysical and quantum chemical studies revealed the presence of equilibrated lowest energy excited states, S_1 and T_1, and the relatively stronger SOC induced by the novel Cu_5 cores in **2a**–**2b**. The mixing of ligand orbitals with d-orbitals of Cu(I) ions was observed from the NBO analyses, implicating the significance of the chloride-bridged Cu atoms present in **2a**–**2b** toward the observed photoluminescence. The combined implementation of both the radiative decay processes brings in the possibility to potentially utilize the low-cost Cu(I) clusters in OLEDs. **2a** has been successfully employed to fabricate the converted LEDs, showing excellent yellow luminescence directing toward the cost-effective Cu(I)-based future OLED productions. Moreover, **2a** has been exploited as an effective photocatalyst in the presence of white LED for the regioselective [3 + 2] cycloadditions of aromatic azides and alkynes, affording the corresponding substituted 1,2,3-triazoles in good to excellent yields under ambient reaction conditions.

METHODS

All manipulations were performed using either standard Schlenk line techniques under an inert argon atmosphere or in an argon-filled MBraun Eco Plus glovebox, where O_2 and H_2O levels were always kept below 0.1 ppm. All glassware was oven-dried (150 °C) before use. Solvents obtained from an MBraun Solvent Purification System (SPS) were further dried by standard methods of refluxing with Na/K alloy for 2 days, followed by vacuum distillation over 4 Å molecular sieves under argon. Cyclic alkyl(amino) carbene (cAAC) salts,[49] free cAACs,[49] cAAC = P–Cl,[13] and $[((Dipp)(Et_2\text{-cAI})P)_2Cs_2(THF)_4]_n$[13] were synthesized according to the literature-reported procedures. Mass spectrometric analyses were performed on an Agilent Technologies (Model: G6545A) Q-TOF LC/MS spectrometer using Dual AJS ESI. The mass spectrometric region of 100–3000 m/z was initially calibrated with the standard tune mix to offer a precision of about 2 ppm. Typical optimized values for the source parameters were capillary 2.5 kV, RF lens 1 kV, and skimmer lens offset 65 V. Aliquots of the solution were injected into the device at 2.0 μL/min. The experimentally obtained isotopic pattern of the complexes was successfully simulated with the suggested pattern corresponding to an empirical formula of a compound using the m-Mass software package.

Synthesis of 2a. In an oven-dried Schlenk flask, orange pure crystals of $[((Cy\text{-cAI})P(Dipp))_2Cs_2(THF)_4]_n$ (**1a**, 100 mg, 0.17 mmol, 3 equiv) and anhydrous CuCl (33 mg, 0.34 mmol, 5 equiv) were taken. Freshly distilled THF (15 mL) was added at room temperature (rt) to obtain a clear yellowish solution, which was stirred overnight, resulting in the formation of a colorless precipitate. The reaction mixture was filtered using a frit to obtain a yellow-colored filtrate, which was concentrated up to 3–4 mL under reduced pressure and kept at −40 °C for crystallization. The rod-shaped bright yellow crystals of $[((Cy\text{-cAI})P(Dipp))_3Cu_5Cl_2]$ (**2a**) suitable for X-ray single-crystal diffraction were formed after 4 weeks in 51% yield (42 mg).

^{1}H NMR (400 MHz, 298 K, CD_2Cl_2): δ 7.34 (d, J = 4 Hz, 1H), 7.30 (d, J = 4 Hz, 1H), 7.24 (d, J = 4 Hz, 1H), 7.19 (d, J = 8 Hz, 1H), 7.15 (d, J = 8 Hz, 1H), 7.11 (broad, 2H), 7.00 (d, J = 8 Hz, 1H), 6.92 (d, J = 4 Hz, 1H), 5.09 (br, 1H), 4.26 (br, 1H), 4.14 (br, 1H), 4.05 (br, 3H), 1.87 (d, J = 12 Hz, 1H), 1.75 (d, J = 4 Hz, 2H), 1.70 (d, J = 8 Hz, 1H), 1.64 (s, 3H), 1.56 (d, J = 4 Hz, 3H), 1.52 (s, 6H), 1.45 (d, J = 8 Hz, 6H), 1.40 (s, 3H), 1.34 (s, 6H), 1.31 (d, J = 4 Hz, 6H), 1.28 (s, 2H), 1.25 (d, J = 8 Hz, 6H), 1.19 (d, J = 8 Hz, 12H), 1.17 (s, 2H), 1.12 (d, J = 8 Hz, 3H), 1.09 (d, J = 8 Hz, 2H), 0.96–0.93 (m, 10H), 0.83 (m, 10H), 0.55 (t, J = 8 Hz, 3H), 0.42 (t, J = 8 Hz, 3H) ppm. ^{31}P NMR (162 MHz, 298 K, CD_2Cl_2): δ −66.1 (dd, J = 105.3, 42.1 Hz), −73.0 (d, J = 98.8 Hz), −99.2 (d, J = 140.9 Hz) ppm. ^{13}C NMR (101 MHz, 273 K, CD_2Cl_2): δ 195.7 (J_{C-P} = 89.8 Hz); $C_{N=C}$, 155.3, 153.2, 133.3, 130.4, 129.2, 128.7, 124.3, 123.5, 71.3, 68.0, 61.0, 47.6, 47.0, 38.7, 32.6, 31.9, 30.0, 26.5, 25.4, 23.4, 23.0, 14.2. Elemental analysis for $C_{69}H_{105}Cl_2Cu_5N_3P_3$ (**2a**): Observed in % (Calcd in %): C, 56.73 (56.84); H, 7.18 (7.26); N, 2.76 (2.88). mp 172–173 °C.

Crystallization 2a. The dark yellow filtrate obtained upon filtering the reaction mixture was concentrated under reduced pressure up to 2 mL and kept at −40 °C in a freezer for one month, from which bright yellow rod-shaped single crystals of cluster **2a** suitable for X-ray diffraction were grown.

Crystallographic Details. Single crystal X-ray data were collected on a Bruker D8 VENTURE diffractometer equipped with a PHOTON III C28 detector using an IμS 3.0 microfocus sealed X-ray source with Molybdenum Kα radiation. A complete data set was collected following the strategies generated using the APEX4 module of the Bruker software suite. The data reduction was carried out using the SAINTPLUS and multiscan absorption correction was performed using the SADABS program.[50] The crystal structures were solved by the intrinsic phasing method (SHELXT)[51] and were refined with full-matrix least-squares on F_2 using the ShelXle[51] plug-in included in APEX 4. All non-hydrogen atoms were refined anisotropically. OLEX2 Version 1.3.0 was used for structure solution and refinement.[52] Ortep-3 was used to produce all the structures' thermal ellipsoid plots.

Photophysical Measurements. All measurements were performed under an argon atmosphere using standard quartz cuvettes (1 × 1 cm cross-section). UV–visible absorption spectra were recorded by using an Agilent Cary Series UV–vis–NIR spectrophotometer. The room temperature and/or low-temperature lifetime, photoluminescence (PL), and absolute quantum yields of **2a**/**2b** in the solid state or in solution were measured in an EDINBURGH FLS1000 photoluminescence spectrometer, attached with an Optistat DN cryostat. All samples for various measurements were prepared inside the glovebox by using a screw cap, an airtight quartz cuvette (1 cm × 1 cm cross-section), or a quartz holder. In each case, initially, we measured the blank, and then again, the same cuvette was taken inside the glovebox, and a specific amount of compound was added for the respective measurements. The concentration of compounds for UV/emission measurements was always kept lower than ca. 2×10^{-5} M.

ASSOCIATED CONTENT

Supporting Information

The Supporting Information is available free of charge at https://pubs.acs.org/doi/10.1021/acs.inorgchem.5c03056.

Experimental details, UV–vis, fluorescence, XPS, FT-IR, and NMR spectra, HRMS, and crystallographic data, computational details, and optimized coordinates (PDF)

Accession Codes

Deposition Nos. 2334709–2334710, 2374018, and 2449539 contain the supplementary crystallographic data for this paper. These data can be obtained free of charge via the joint

https://doi.org/10.1021/acs.inorgchem.5c03056
Inorg. Chem. XXXX, XXX, XXX–XXX

Cambridge Crystallographic Data Centre (CCDC) and Fachinformationszentrum Karlsruhe Access Structures service.

AUTHOR INFORMATION

Corresponding Authors

Aloke Das − *Department of Chemistry, Indian Institute of Science Education and Research (IISER) Pune, Pashan, Pune 411008, India;* orcid.org/0000-0002-2124-0631; Email: a.das@iiserpune.ac.in

Di Sun − *School of Chemistry and Chemical Engineering, Shandong University, Ji'nan 250100, People's Republic of China;* orcid.org/0000-0001-5966-1207; Email: dsun@sdu.edu.cn

Sudipta Roy − *Department of Chemistry, Indian Institute of Science Education and Research (IISER) Tirupati, Tirupati 517619, India;* orcid.org/0000-0002-5883-4329; Email: roy.sudipta@iisertiruapti.ac.in

Authors

Asutosh Patra − *Department of Chemistry, Indian Institute of Science Education and Research (IISER) Tirupati, Tirupati 517619, India;* orcid.org/0000-0002-8570-3121

Kishor Shinde − *Department of Chemistry, Indian Institute of Science Education and Research (IISER) Tirupati, Tirupati 517619, India*

Sourav Mandal − *Department of Chemistry, Indian Institute of Science Education and Research (IISER) Pune, Pashan, Pune 411008, India;* orcid.org/0009-0009-2307-3804

Ashwath Kudlu − *Department of Chemistry, Indian Institute of Science Education and Research (IISER) Tirupati, Tirupati 517619, India;* orcid.org/0000-0002-6740-9607

Wei-dan Si − *School of Chemistry and Chemical Engineering, Shandong University, Ji'nan 250100, People's Republic of China;* orcid.org/0000-0002-4879-9283

Maria Francis − *Department of Chemistry, Indian Institute of Science Education and Research (IISER) Tirupati, Tirupati 517619, India;* orcid.org/0000-0002-0506-4885

Complete contact information is available at: https://pubs.acs.org/10.1021/acs.inorgchem.5c03056

Notes

The authors declare no competing financial interest.

ACKNOWLEDGMENTS

S.R. acknowledges STARS-IISC, MoE, Govt. of India (MoE-STARS/STARS-2/2023-0666), and IISER Tirupati for the generous financial support and instrumental facilities. A.P. and K.S. thank IISER Tirupati for their SRF and JRF, respectively. M.F. thanks CSIR for SRF. S.M. and A.D. acknowledge the computational support and resources from the "PARAM Brahma Facility" under the National Supercomputing Mission, Govt. of India, at IISER, Pune. S.M. also thanks IISER Pune for the JRF. We thank Dr. J.K., IISER Tirupati, for generous support in facilitating all photophysical studies. D.S. thanks the financial support from the National Natural Science Foundation of China (Grant Nos. 22171164, 22325105, 52261135637, 92361301).

REFERENCES

(1) Uoyama, H.; Goushi, K.; Shizu, K.; Nomura, H.; Adachi, C. Highly Efficient Organic Light-emitting Diodes from Delayed Fluorescence. *Nature* **2012**, *492*, 234−238.

(2) Zhang, Q.; Li, J.; Shizu, K.; Huang, S.; Hirata, S.; Miyazaki, H.; Adachi, C. Design of Efficient Thermally Activated Delayed Fluorescence Materials for Pure Blue Organic Light Emitting Diodes. *J. Am. Chem. Soc.* **2012**, *134*, 14706−14709.

(3) Dias, F. B.; Bourdakos, K. N.; Jankus, V.; Moss, K. C.; Kamtekar, K. T.; Bhalla, V.; Santos, J.; Bryce, M. R.; Monkman, A. P. Triplet Harvesting with 100% Efficiency by Way of Thermally Activated Delayed Fluorescence in Charge Transfer OLED Emitters. *Adv. Mater.* **2013**, *25*, 3707−3714.

(4) Tian, W.; Zhang, C.; Paul, S.; Si, W.; Wang, Z.; Sun, P.; Anoop, A.; Tung, C.; Sun, D. Lattice Modulation on Singlet-Triplet Splitting of Silver Cluster Boosting Near Unity Photoluminescence Quantum Yield. *Angew. Chem., Int. Ed.* **2025**, *64*, No. e202421656.

(5) Chandrashekar, P.; Sardar, G.; Sengupta, T.; Reber, A. C.; Mondal, P. K.; Kabra, D.; Khanna, S. N.; Deria, P.; Mandal, S. Modulation of Singlet-Triplet Gap in Atomically Precise Silver Cluster-Assembled Material. *Angew. Chem., Int. Ed.* **2024**, *63*, No. e202317345.

(6) Biswas, S.; Das, A. K.; Mandal, S. Surface Engineering of Atomically Precise M(I) Nanoclusters: From Structural Control to Room Temperature Photoluminescence Enhancement. *Acc. Chem. Res.* **2023**, *56*, 1838−1849.

(7) Leitl, M. J.; Küchle, F.; Mayer, H. A.; Wesemann, L.; Yersin, H. Brightly Blue and Green Emitting Cu(I) Dimers for Singlet Harvesting in OLEDs. *J. Phys. Chem. A* **2013**, *117*, 11823−11836.

(8) Zhang, L.; Cheah, K. W. Thermally Activated Delayed Fluorescence Host for High Performance Organic Light-Emitting Diodes. *Sci. Rep.* **2018**, *8*, 8832−8837.

(9) Zhang, M.; Dong, X.; Wang, Z.; Li, H.; Li, S.; Zhao, X.; Zang, S. AIE Triggers the Circularly Polarized Luminescence of Atomically Precise Enantiomeric Copper(I) Alkynyl Clusters. *Angew. Chem., Int. Ed.* **2020**, *59*, 10052−10058.

(10) Wang, Z.; Sun, H.-T.; Kurmoo, M.; Liu, Q.-Y.; Zhuang, G.-L.; Zhao, Q.-Q.; Wang, X.-P.; Tung, C.-H.; Sun, D. Carboxylic Acid Stimulated Silver Shell Isomerism in a Triple Core−Shell Ag_{84} Nanocluster. *Chem. Sci.* **2019**, *10*, 4862−4867.

(11) Yuan, Z.; Wang, Z.; Han, B.; Zhang, C.; Zhang, S.; Zhu, Z.; Yu, J.; Li, T.; Li, Y.; Tung, C.; Sun, D. Ag_{22} Nanoclusters with Thermally Activated Delayed Fluorescence Protected by Ag/Cyanurate/Phosphine Metalla-macrocyclic Monolayers through In-Situ Ligand Transesterification. *Angew. Chem., Int. Ed.* **2022**, *61*, No. e202211628.

(12) Xu, C.; Jin, Y.; Fang, H.; Zheng, H.; Carozza, J. C.; Pan, Y.; Wei, P.; Zhang, Z.; Wei, Z.; Zhou, Z.; Han, H. A High-Nuclearity Copper Sulfide Nanocluster [S-Cu_{50}] Featuring a Double-Shell Structure Configuration with Cu(II)/Cu(I) Valences. *J. Am. Chem. Soc.* **2023**, *145*, 25673−25685.

(13) Liu, X.; Xu, W. W.; Huang, X.; Wang, E.; Cai, X.; Zhao, Y.; Li, J.; Xiao, M.; Zhang, C.; Gao, Y.; Ding, W.; Zhu, Y. De Novo Design of $Au_{36}(SR)_{24}$ Nanoclusters. *Nat. Commun.* **2020**, *11*, 3349.

(14) Nag, E.; Francis, M.; Putta, D.; Roy, S. Isolation of (Aryl)(Imino) Phosphide and (Aryl)(Phosphaalkene) Amide Complexes of Alkali Metals from Carbene-Phosphinidenes under Reductive-Thermal Rearrangements. *Chem. - Eur. J.* **2023**, *29*, No. e202302120.

(15) Caddick, S.; Cloke, F. G. N.; Hitchcock, P. B.; de K Lewis, A. K. Unusual Reactivity of a Nickel N-Heterocyclic Carbene Complex: ^{tert}-Butyl Group Cleavage and Silicone Grease Activation. *Angew. Chem., Int. Ed.* **2004**, *43*, 5824−5827.

(16) Sculfort, S.; Braunstein, P. Intramolecular d_{10}−d_{10} Interactions in Heterometallic Clusters of the Transition Metals. *Chem. Soc. Rev.* **2011**, *40*, 2741−2760.

(17) Adiraju, V. A. K.; Yousufuddin, M.; Rasika Dias, H. V. Copper(I), Silver(I) and Gold(I) Complexes of N-Heterocyclic Carbene-Phosphinidene. *Dalton Trans.* **2015**, *44*, 4449−4454.

(18) Dutta, C.; Maniappan, S.; Kumar, J. Dual Emissive Optically Active Gold Nanoclusters Endowed with Circularly Polarized Phosphorescence. *Chem. Commun.* **2023**, *59*, 13735−13738.

(19) Lee, C.; Yang, W.; Parr, R. G. Development of the Colle-Salvetti Correlation-energy Formula into a Functional of the Electron

Density. *Phys. Rev. B: Condens. Matter Mater. Phys.* **1988**, *37*, 785−789.
(20) Becke, A. D. Density-functional Exchange-energy Approximation with Correct Asymptotic Behavior. *Phys. Rev. A: At., Mol., Opt. Phys.* **1988**, *38*, 3098−3100.
(21) Weigend, F.; Ahlrichs, R. Balanced Basis Sets of Split Valence, Triple Zeta Valence and Quadruple Zeta Valence Quality for H to Rn: Design and Assessment of Accuracy. *Phys. Chem. Chem. Phys.* **2005**, *7*, 3297−3305.
(22) Spackman, P. R.; Turner, M. J.; McKinnon, J. J.; Wolff, S. K.; Grimwood, D. J.; Jayatilaka, D.; Spackman, M. A. CrystalExplorer: A Program for Hirshfeld Surface Analysis, Visualization and Quantitative Analysis of Molecular Crystals. *J. Appl. Crystallogr.* **2021**, *54*, 1006−1011.
(23) Czerwieniec, R.; Leitl, M. J.; Homeier, H. H. H.; Yersin, H. Cu(I) Complexes−Thermally Activated Delayed Fluorescence. Photophysical Approach and Material Design. *Coord. Chem. Rev.* **2016**, *325*, 2−28.
(24) Zhang, L.-M.; Xie, M.; Wei, H.-Z.; Yuan, S.-F.; Li, D.-S.; Wu, T. N.-. Heterocyclic Carbene-Stabilized Cu_9 Clusters with Combined Thermally Activated Delayed Fluorescence and Phosphorescence. *Inorg. Chem. Front.* **2024**, *11*, 2498−2507.
(25) Shafikov, M. Z.; Suleymanova, A. F.; Schinabeck, A.; Yersin, H. Dinuclear Ag(I) Complex Designed for Highly Efficient Thermally Activated Delayed Fluorescence. *J. Phys. Chem. Lett.* **2018**, *9*, 702−709.
(26) Schinabeck, A.; Rau, N.; Klein, M.; Sundermeyer, J.; Yersin, H. Deep Blue-Emitting Cu(I) Tripod Complexes. Design of High Quantum Yield Materials Showing TADF-Assisted Phosphorescence. *Dalton Trans.* **2018**, *47*, 17067−17076.
(27) Gao, X.; Bai, S.; Fazzi, D.; Niehaus, T.; Barbatti, M.; Thiel, W. Evaluation of Spin-Orbit Couplings with Linear-Response Time-Dependent Density Functional Methods. *J. Chem. Theory Comput.* **2017**, *13*, 515−524.
(28) Chen, X.-L.; Yu, R.; Wu, X.-Y.; Liang, D.; Jia, J.-H.; Lu, C.-Z. Correction: A Strongly Greenish-Blue-Emitting Cu_4Cl_4 Cluster with an Efficient Spin−Orbit Coupling (SOC): Fast Phosphorescence versus Thermally Activated Delayed Fluorescence. *Chem. Commun.* **2016**, *52*, 7738.
(29) Chatterjee, A.; Chatterjee, J.; Sappati, S.; Tanwar, R.; Ambhore, M. D.; Arfin, H.; Umesh, R. M.; Lahiri, M.; Mandal, P.; Hazra, P. Engineering TADF, Mechano-chromism, and Second Harmonic Up-Conversion Properties in Regio-isomeric Substitution Space. *Chem. Sci.* **2023**, *14*, 13832−13841.
(30) Reed, A. E.; Curtiss, L. A.; Weinhold, F. Intermolecular Interactions from a Natural Bond Orbital, Donor-acceptor Viewpoint. *Chem. Rev.* **1988**, *88*, 899−926.
(31) Reed, A. E.; Weinstock, R. B.; Weinhold, F. Natural Population Analysis. *J. Chem. Phys.* **1985**, *83*, 735−746.
(32) Wiberg, K. B. Application of the Pople-santry-segal CNDO Method to the Cyclopropylcarbinyl and Cyclobutyl Cation and to Bicyclobutane. *Tetrahedron* **1968**, *24*, 1083−1096.
(33) Glendening, E. D.; Landis, C. R.; Weinhold, F. NBO 6.0: Natural Bond Orbital Analysis Program. *J. Comput. Chem.* **2013**, *34*, 1429−1437.
(34) Bader, R. F. W. *Atoms in Molecules: A Quantum Theory*; Clarendon Press: Oxford, 1990.
(35) Bader, R. F. W. A Quantum Theory of Molecular Structure and Its Applications. *Chem. Rev.* **1991**, *91*, 893−928.
(36) Bader, R. F. W. Atoms in Molecules. *Acc. Chem. Res.* **1985**, *18*, 9−15.
(37) Miertuš, S.; Scrocco, E.; Tomasi, J. Electrostatic Interaction of a Solute with a Continuum. A Direct Utilizaion of AB Initio Molecular Potentials for the Prevision of Solvent Effects. *J. Chem. Phys.* **1981**, *55*, 117−129.
(38) Tomasi, J.; Mennucci, B.; Cammi, R. Quantum Mechanical Continuum Solvation Models. *Chem. Rev.* **2005**, *105*, 2999−3094.
(39) Hofbeck, T.; Monkowius, U.; Yersin, H. Highly Efficient Luminescence of Cu(I) Compounds: Thermally Activated Delayed Fluorescence Combined with Short-Lived Phosphorescence. *J. Am. Chem. Soc.* **2015**, *137*, 399−404.
(40) Martin, R. L. Natural Transition Orbitals. *J. Chem. Phys.* **2003**, *118*, 4775−4777.
(41) Moitra, T.; Karak, P.; Chakraborty, S.; Ruud, K.; Chakrabarti, S. Behind the Scenes of Spin-Forbidden Decay Pathways in Transition Metal Complexes. *Phys. Chem. Chem. Phys.* **2021**, *23*, 59−81.
(42) Yan, J.; Teo, B. K.; Zheng, N. Surface Chemistry of Atomically Precise Coinage−Metal Nanoclusters: From Structural Control to Surface Reactivity and Catalysis. *Acc. Chem. Res.* **2018**, *51*, 3084−3093.
(43) Wu, Z. G.; Liao, X. J.; Yuan, L.; Wang, Y.; Zheng, Y. X.; Zuo, J. L.; Pan, Y. Visible-Light-Mediated Click Chemistry for Highly Regioselective Azide−Alkyne Cycloaddition by a Photoredox Electron-Transfer Strategy. *Chem. - Eur. J.* **2020**, *26*, 5694−5700.
(44) Meldal, M.; Tornøe, C. W. CuCatalyzed Azide-Alkyne Cycloaddition. *Chem. Rev.* **2008**, *108*, 2952−3015.
(45) González-Lainez, M.; Gallegos, M.; Munarriz, J.; Azpiroz, R.; Passarelli, V.; Jiménez, M. V.; Pérez-Torrente, J. J. Copper-Catalyzed Azide-Alkyne Cycloaddition (CuAAC) by Functionalized NHC-Based Polynuclear Catalysts: Scope and Mechanistic Insights. *Organometallics* **2022**, *41*, 2154−2169.
(46) Tornøe, C. W.; Christensen, C.; Meldal, M. Peptidotriazoles on Solid Phase: [1,2,3]-Triazoles by Regiospecific Copper(I)-Catalyzed 1,3-Dipolar Cycloadditions of Terminal Alkynes to Azides. *J. Org. Chem.* **2002**, *67*, 3057−3064.
(47) Raghavendra, M. S.; Lam, Y. Regiospecific Solid-Phase Synthesis of Substituted 1,2,3-Triazoles. *Tetrahedron Lett.* **2004**, *45*, 6129−6132.
(48) Jin, L.; Tolentino, D. R.; Melaimi, M.; Bertrand, G. Isolation of Bis(Copper) Key Intermediates in Cu-catalyzed Azide-alkyne "Click Reaction". *Sci. Adv.* **2015**, *1*, No. e1500304.
(49) Lavallo, V.; Canac, Y.; Präsang, C.; Donnadieu, B.; Bertrand, G. Stable Cyclic (Alkyl)(Amino)Carbenes as Rigid or Flexible, Bulky, Electron-Rich Ligands for Transition-Metal Catalysts: A Quaternary Carbon Atom Makes the Difference. *Angew. Chem., Int. Ed.* **2005**, *44*, 5705−5709.
(50) Bruker. *APEX4, SAINT and SADABS*; Bruker AXS Inc.: Madison, WI, USA, 2021.
(51) Sheldrick, G. M. Crystal Structure Refinement with SHELXL. *Acta Crystallogr., Sect. C: Struct. Chem.* **2015**, *71*, 3−8.
(52) Dolomanov, O. V.; Bourhis, L. J.; Gildea, R. J.; Howard, J. A. K.; Puschmann, H. OLEX2: A Complete Structure Solution, Refinement and Analysis Program. *J. Appl. Crystallogr.* **2009**, *42*, 339−341.

https://doi.org/10.1021/acs.inorgchem.5c03056
Inorg. Chem. XXXX, XXX, XXX−XXX